



RESEARCH LETTER

10.1002/2016GL069603

Key Points:

- Large intermediate-depth earthquakes in Hindu Kush concentrate in a small volume
- The last three $M \geq 7$ events show diverse rupture processes, but their main subevents appear to recur on the same fault patch
- The recurrence requires significant slab internal deformation such as necking due to a fast sinking slab

Supporting Information:

- Supporting Information S1

Correspondence to:

Z. Zhan,
zwzhan@gps.caltech.edu

Citation:

Zhan, Z., and H. Kanamori (2016), Recurring large deep earthquakes in Hindu Kush driven by a sinking slab, *Geophys. Res. Lett.*, 43, 7433–7441, doi:10.1002/2016GL069603.

Received 17 MAY 2016

Accepted 29 JUN 2016

Accepted article online 4 JUL 2016

Published online 16 JUL 2016

Recurring large deep earthquakes in Hindu Kush driven by a sinking slab

Zhongwen Zhan¹ and Hiroo Kanamori¹

¹Seismological Laboratory, Division of Geological and Planetary Sciences, California Institute of Technology, Pasadena, California, USA

Abstract Hindu Kush subduction zone produces large intermediate-depth earthquakes within a small volume every 10–15 years. Here we study the last three $M \geq 7$ events within the cluster and find complex and diverse rupture processes. However, their main subevents appear to recur on the same fault patch, dipping 70° to the south. This recurrence requires an average of 9.6 cm/yr slip rate on the patch, much higher than the ~1 cm/yr surface convergence rate measured geodetically. The high slip rate is likely caused by significant slab internal deformation, such as localized slab stretching/necking. We infer that the Hindu Kush subducted slab below 210 km is sinking through the mantle at a vertical rate of 10 cm/yr.

1. Introduction

Hindu Kush is one of the most seismically active regions in the world, with frequent large ($M \geq 7$) earthquakes at about 200 km depth. The latest one was the 26 October 2015 M_w 7.5 earthquake, which caused >400 casualties, only 13 years after the last M_w 7.3 earthquake in 2002 at almost the same location. The anomalously high seismic activity at depth has been noticed for a long time. For example, *Gutenberg and Richter* [1954] wrote in *Seismicity of the Earth*: “Among the Hindu Kush earthquakes at intermediate depth the larger shocks are abnormally frequent, ... Most of the epicenters are at nearly the same point near 36.5 N, 70.5 E (230 km).” The Global Centroid-Moment-Tensor (GCMT) catalog and the recently compiled ISC-GEM catalog [Storchak *et al.*, 2013], in which large earthquakes’ locations and magnitudes are recalibrated with special care [Di Giacomo *et al.*, 2015], show that $M \geq 7$ Hindu Kush deep earthquakes occurred semiregularly, once every 10–15 years (Figure 1). For 1900–1950, when the ISC-GEM catalog is not complete for $M7$ s, the Gutenberg-Richter catalog includes 10 more $M7$ events (gray dots in Figure 1b), suggesting that the activity prior to 1950 may have been even higher than recent years. However, the 10 events’ magnitudes may not be well calibrated.

The Hindu Kush deep earthquakes are concentrated in a small volume (Figure 1a) and often called “earthquake nest” [Pavlis and Hamburger, 1991; Pegler and Das, 1998; Pavlis and Das, 2000; Prieto *et al.*, 2012]. In particular, Sippl *et al.* [2013] relocated small earthquakes in Hindu Kush from 2008 to 2010 using a local seismic network and found that the deep events form a band only 15 km thick. For the $M \geq 7$ events in the last century, epicenters and centroids from various catalogs are all located within 50 km from each other. A notable exception is the 1983 M_w 7.4 GCMT centroid, which is offset to the north by >50 km, even though its epicenter in the U.S. Geological Survey (USGS) Preliminary Determination of Epicenters (PDE) bulletin is still close to the other events (Figure 1a). In Figure 1c we compare the long-period ($T > 20$ s) waveforms between the 1983 and the 2015 events at four stations, aligned on the direct P waves. We find that all the later phases including sP , PP , S , SS , and surface waves are well aligned and have similar waveforms. If the 1983 centroid is actually displaced from the other events as shown in Figure 1a, these later phases would have 5–10 s misalignments, easily visible in Figure 1c. Therefore, we conclude that the 1983 earthquake centroid location and depth are very close to the other $M > 7$ events.

Why large deep earthquakes in Hindu Kush are so frequent and concentrated is unclear. The earthquake locations and focal mechanisms suggest they are intraplate earthquakes within the subducted oceanic plate, loaded by slab pulling stress [Pegler and Das, 1998]. The plate convergence rate measured on the surface is very low, only ~1 cm/yr, as part of the 3–5 cm/yr overall shortening distributed across a wide area [Ischuk *et al.*, 2013]. Therefore, significant slab internal deformation is required to cause the active seismicity. Lister *et al.* [2008] proposed that the Hindu Kush earthquake nest is a manifestation of active slab stretching (necking) due to the negative buoyancy of a hanging “slablet.” But the required slab-stretching rate is not

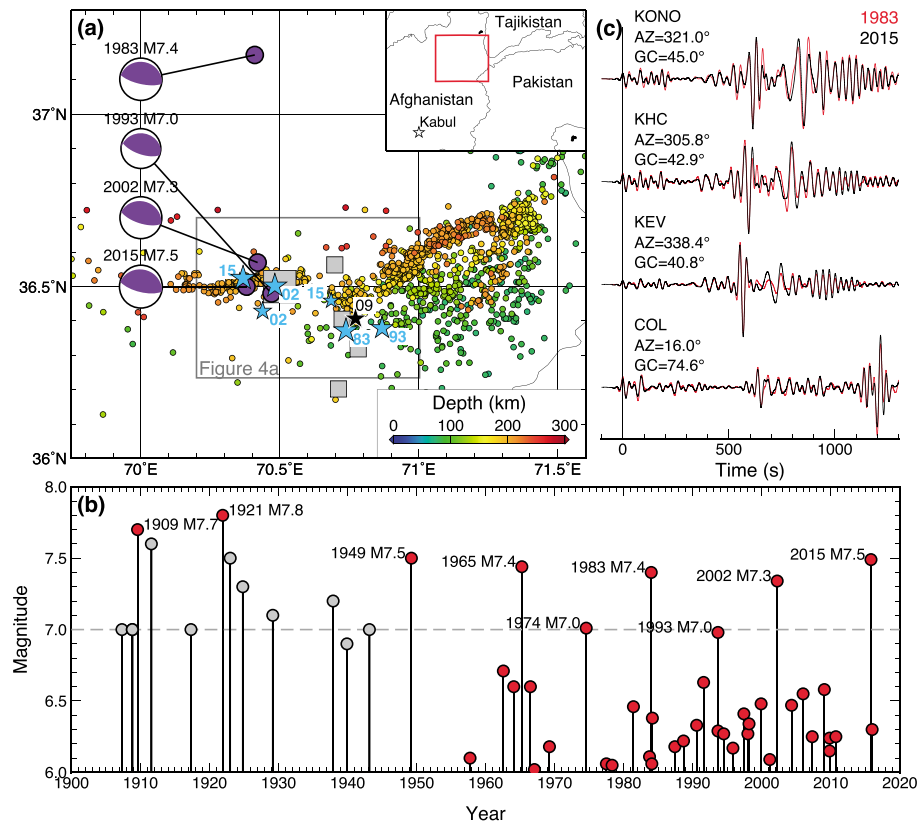


Figure 1. Hindu Kush seismicity. (a) Earthquake locations in the Hindu Kush area. The small dots colored by depth are 2008–2010 deep (>70 km) seismicity relocated by Sippl *et al.* [2013]. Five $M > 7$ earthquakes before 1983 in the ISC-GEM catalog are displayed as gray squares, while the large gray square at (70.5°E, 36.5°N) contains 10 events located by Gutenberg and Richter [1954]. The GCMT solutions and USGS PDE epicenters of the last four $M > 7$ events are shown as purple dots and light blue stars, respectively. Because the 2002 and 2015 $M7$ events are both registered as two earthquakes, there are two light blue stars for each event. The 1983 centroid is >50 km to the north of the other centroids, while its epicenter does not have such an offset. The black star represents the 2009 reference event used in the directivity analysis. The gray rectangle marks the area plotted in Figure 4a. (b) Magnitude-time plot of $M > 6.0$ Hindu Kush deep earthquakes, based on the GCMT, ISC-GEM catalogs (red), and the Gutenberg-Richter catalog (gray). This study focuses on events with magnitude around and above 7.0, which is marked by the gray dashed line. (c) Comparison of the long-period ($T > 20$ s) waveforms between the 1983 $M7.4$ event and the 2015 $M7.5$ event, at four stations. The waveforms are aligned on the P waves, and amplitudes are normalized. The perfect alignments in later phases suggest that the GCMT centroid location of the 1983 event in Figure 1a is mislocated.

constrained, and whether the rate is physically plausible is unknown. To quantify the slab-stretching picture, in this paper we study the last three $M \geq 7$ events with globally distributed digital seismic data in detail: the 9 August 1993 M_w 7.0 event, the 3 March 2002 M_w 7.3 event, and the 26 October 2015 M_w 7.5 event (Table S1 in the supporting information). We aim to answer the following questions: Are the earthquakes recurring (at least partially) on the same fault plane? What is the average slip rate on the fault plane? Is the corresponding slab-stretching rate plausible for the slab negative buoyancy and mantle viscosity?

2. Depths and Focal Mechanisms

Earthquake depths are often difficult to constrain with only first-arrival data or long-period waveforms. The GCMT solutions of the 1993, 2002, and 2015 events have similar horizontal locations (Figure 1a) but different depths: the difference in depth between the 2002 and 2015 events is more than 30 km (Figure 2a), too large for the events to overlap significantly. To resolve whether the three events possibly ruptured the same fault plane, we first apply the cut-and-paste (CAP) method to determine their point source solutions [Zhu and Helmberger, 1996; Zhan *et al.*, 2012]. We filter teleseismic P and SH waveforms with a pass band of 20–100 s, a period band long enough for the events to be approximated as point sources and short enough for the

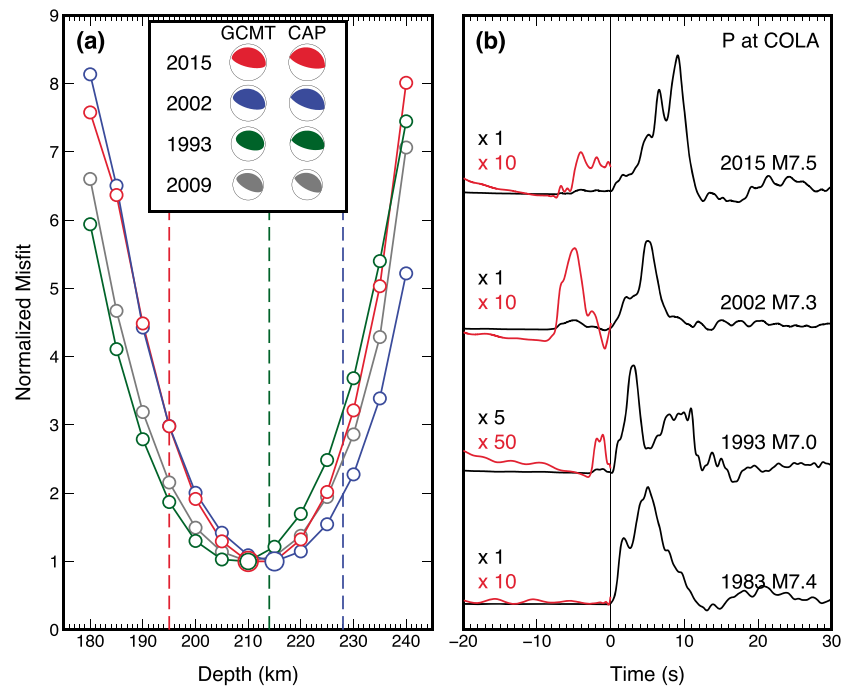


Figure 2. Point source solutions and broadband waveforms. (a) Cut-and-paste (CAP) inversion for the 1993, 2002, and 2015 events and the 2009 reference event, using teleseismic P and SH waves. The dashed lines indicate the three large events' depths based on the GCMT catalog, different by more than 10 km between any pair. The dots connected by solid lines show depth misfit curves normalized by the optimal solutions, marked as larger dots. The optimal depths of the four events are within 5 km. The optimal focal mechanisms are shown in the inset, together with the GCMT moment tensors. (b) Broadband P displacement seismograms of the last four $M \geq 7$ events recorded by station COLA, aligned by the onsets of high-amplitude waves. The waveforms before the onsets are amplified by a factor of 10 to highlight the weak precursors. The numbers to the left of each trace are the amplification factors.

depth phases to be separate from the direct phases. Synthetic waveforms are computed using the PREM model. We then grid-search depths and focal mechanisms by best fitting the waveforms. Figure 2a shows the misfit curves, and the optimal depths are 210 km for the 1993 and 2015 events, and 215 km for the 2002 event, with a 5 km grid-search step size. The CAP-inverted focal mechanisms are similar to the GCMT moment tensor solutions (Figure 2a inset), with one nodal plane dipping $\sim 70^\circ$ toward the south and another nodal plane dipping $\sim 20^\circ$ toward the north. From this comparison we conclude that the three events have similar centroid locations, depths, and focal mechanisms.

However, the three events are not repeaters in the sense that their rupture patterns are identical. Figure 2b displays their broadband P displacement waveforms at the same station COLA. Besides the differences in earthquake moment, the three events do not have the same waveforms, suggesting that at least the kinematic rupture processes are different. Interestingly, the three events also all have weak but clear precursory arrivals (zoomed red traces in Figure 2b), while the 1983 event does not. *Poli et al.* [2016] report that the initiation phase is inefficient in generating seismic waves. Rupture processes producing the weak precursors are difficult to image, and the later main slip patches can potentially be far away from the earthquake hypocenters. We will need to derive subevent models to get a clearer image of their rupture processes. We will follow a two-step procedure: (1) display the dominant features in waveform data and determine the first-order rupture processes by directivity analysis and (2) use the models produced in step 1 as initial models to conduct waveform inversions for subevent models.

3. Directivity Analysis

The directivity analysis performed in this study is similar to that described in *Zhan et al.* [2014]. As shown by Figure 3, we first arrange the teleseismic P waveforms by their horizontal directivity parameters defined by $-\cos(\theta - \theta_r)/c_p$, where θ_r is an assumed unilateral rupture direction from a reference point, θ and c_p are

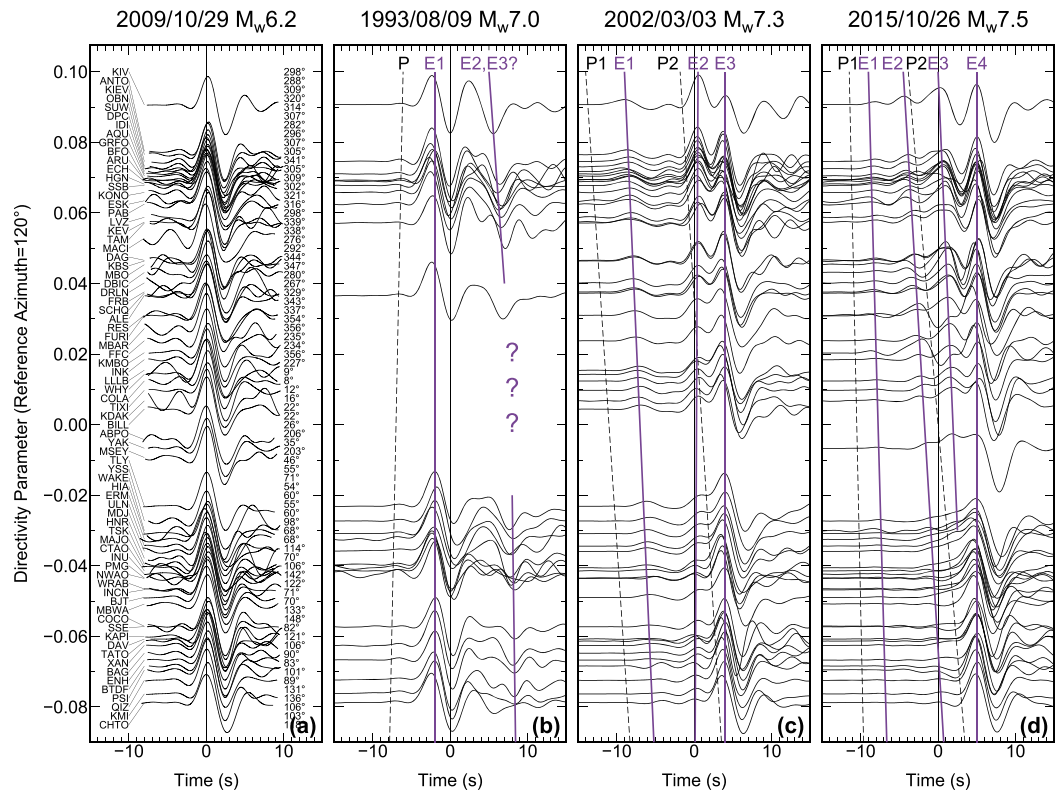


Figure 3. Directivity analysis. (a) Teleseismic *P* waveforms of the 2009 reference event, low-pass filtered at 3 s, and aligned by cross correlations. Station names and azimuths are shown to the left and right, respectively. (b–d) Directivity plots of the 1993, 2002, and 2015 events, after applying the travel time corrections derived from the 2009 reference event in Figure 3a. The waveforms are arranged by their directivity parameters with the reference point at the relocated 2009 epicenter (instead of their own epicenters) and an assumed rupture azimuth of 120°. Seismograms are flipped to ensure consistent polarities. The thick purple lines with “E” labels indicate arrivals of major subevents, and the black dashed lines with “P” labels are predicted arrivals of their USGS PDE solutions (two for the 2002 and 2015 events).

station azimuth and *P* wave phase speed. Commonly, in directivity plots, the *P* waveforms are aligned at the onsets of *P* waves so that the epicenter is taken as the reference point. But if the *P* onsets are difficult to pick consistently for all the stations due to noise or weak initiation phases, we may align the *P* waves by the theoretical *P* arrival times corrected for the travel time anomaly along the path. Depending on how the travel time predictions and path corrections are derived, the reference point in space may move from the epicenter. If the assumed rupture direction, θ_r , is correct, subevents can be identified by straight lines with slopes giving the distance of the subevent measured from the reference point in the azimuth of θ_r . For the three Hindu Kush events, it is difficult to accurately pick the *P* onsets due to their weak initiation phases shown in Figure 2b. Furthermore, the relative locations of the USGS PDE epicenters may have large uncertainties, which make the comparison among the three earthquakes ambiguous if we use the epicenter as the reference point.

We accordingly modify the directivity analysis using a nearby event as reference. As the reference event, we use the 26 October 2009 M_w 6.2 earthquake (black star in Figure 1a) relocated by *Sippl et al.* [2013] using a local seismic network. Our CAP inversion demonstrates that the 2009 event is similar to the three large events in depth and focal mechanism (Figure 2a) and serves as a good calibration event. To avoid involving rupture complexities within the 2009 event, we low-pass filter all the data at 3 s. Figure 3a shows the directivity plot for the 2009 event, aligned at the largest phase by cross correlations. This plot is used to determine along-path travel time corrections. We then apply the travel time corrections to the directivity plots of the three large events. We align their *P* waveforms by the theoretical *P* travel times based on their own origin times but the 2009 event’s epicenter with the travel time corrections. Therefore, the reference points for all three large events are the same, at the 2009 epicenter. We grid-search rupture direction θ_r with a 2° interval and visually inspect all the directivity plots for the θ_r range showing overall best linear alignments. The optimal

θ_r is around 120° , roughly parallel to the fault strikes, and the directivity plots are displayed in Figures 3b–3d. For comparison, Figure S1 shows the directivity plots without travel time correction. The waveform alignments shown in Figure 3 are much more coherent than the ones shown in Figure S1. Due to the change in the reference points, the time axes in Figures 3 and S1 are somewhat arbitrary, but only the relative timing of subevents is important here.

The main P wave pulses of the 1993 M_w 7.0 earthquake are aligned vertically as subevent E1 (Figure 3b), which means that E1 is located close to the 2009 reference event. The predicted arrival times based on the USGS PDE solution (light blue star in Figure 1a) are plotted as the black dashed line in Figure 3b, which matches the precursory arrivals well. About 5–10 s after E1, another (possibly two) group of coherent phases arrive without aligning on straight lines, suggesting additional subevent(s) not located along the assumed rupture azimuth of 120° . Unfortunately, a major azimuthal gap makes it difficult to locate them accurately.

We identify three subevents for the 2002 M_w 7.3 event (Figure 3c). Subevent E1 has a negative slope, suggesting a location about 30 km to the $N60^\circ W$ (opposite to the assumed θ_r) of the 2009 event. Later, large subevents E2 and E3 both have nearly vertical alignments, hence are located near the 2009 event. Overall, the 2002 event ruptured unilaterally along the assumed θ_r , 120° . In the USGS PDE catalog, the 2002 event is registered as two earthquakes (Figure 1a), whose predicted arrival times are plotted as the black dashed lines P1 and P2 in Figure 3c. While P1 is subparallel to E1, “mainshock” P2 is not parallel to E2 and E3 but has a negative slope. This appears to be a mislocation of the “mainshock” epicenter P2 caused by the difficulty in picking the “mainshock” onsets within the precursory arrivals from E1.

The 2015 M_w 7.5 event, with its 10 s long precursory arrivals, is also listed as two events, P1 and P2, in the USGS PDE catalog (Figure 1a). Epicenter P1 is located close to the 2009 event, while epicenter P2 is ~ 30 km toward the west. This geometry is roughly consistent with subevents E1 and E2 (Figure 3d). A large subevent E3 occurred close to E2, but with a slightly steeper slope, implying a rupture backward to the east. Soon after E3, subevent E4 ruptured back in the epicenter area close to the 2009 event, with a vertical moveout. Due to the small temporal separation between E3 and E4, their waveforms merge together at the stations toward the east (bottom portion of Figure 3d).

In summary, the three events show diverse and complex rupture processes. The 1993 event had only weak directivity, the 2002 event ruptured mostly toward the east, and the 2015 event first ruptured toward the west and then backward to the east. However, major arrivals in the directivity plots are aligned nearly vertically, suggesting major subevents of all three earthquakes locate close to the 2009 reference event, except 2015.E3 to the west.

4. Subevent Models

While the directivity analysis reveals the essential features (e.g., main subevents, overall rupture directions) of the three events, quantitative details regarding the number of subevents, the precise locations, timings, and the moments of the subevents must be derived from waveform inversion. Here we use a subevent algorithm similar to that in Zhan *et al.* [2014], to simultaneously invert the P waveforms shown in Figure 3 (after travel time corrections) for multiple subevent centroid locations, centroid times, and moments. For each set of subevent locations and times, we predict their arrival times at each station, and then assume Gaussian-shaped source-time-functions (STFs) centered at the predicted times, and determine the best fitting durations and amplitudes. Subevent moment is calculated posteriorly as proportional to the area beneath its average STF. We refer the readers to Zhan *et al.* [2014] for more details on the method, and here we only note one change in this application. In Zhan *et al.* [2014], subevent durations and amplitudes are estimated independently for each station to accommodate possible path and site effects. Because the velocity seismograms used here are low-pass filtered at 3 s, the sharpness of pulses is largely smeared. Therefore, we simplify the method by assuming that observed subevent durations τ_{ij} at the j th station from the i th subevent follow a cosine azimuth pattern $\tau_{ij} = \tau_i + \Delta\tau_i \cos(\varphi_j - \varphi_i)$, where τ_i is subevent duration, τ_j is station azimuth. We include $\Delta\tau_i$ and φ_i as new variables in the nonlinear inversion. This simplification improves the efficiency and robustness of inversions.

Figure 4a and Table S1 describe the subevent models. With three subevents for the 1993 and 2002 events, and four subevents for the 2015 event, we are able to fit the teleseismic P waveforms remarkably well (see Figure 5). The 1993 event ruptured its largest $M6.8$ subevent E1 slightly south of the 2009 event, and then

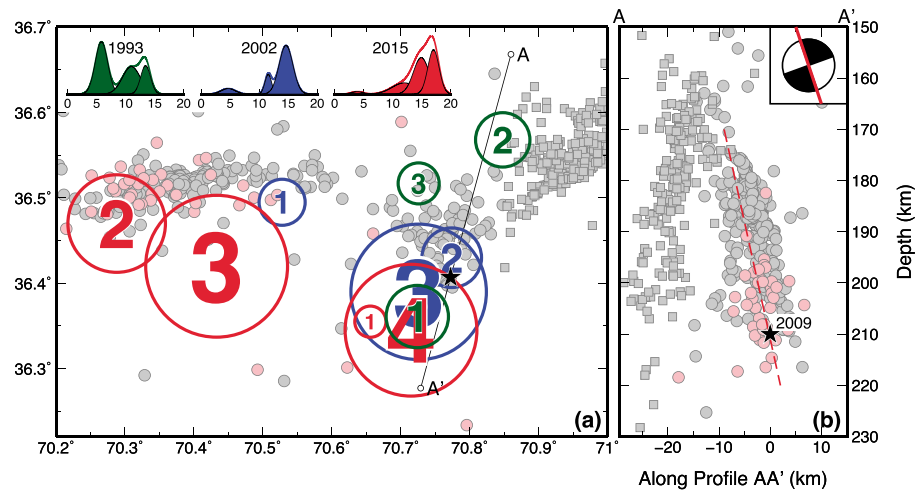


Figure 4. Subevent models and fault plane. (a) Subevents of the 1993, 2002, and 2015 earthquakes are shown as circles numbered sequentially, with sizes proportional to the subevent moments. Moment rate functions are displayed in the top left in the same colors. Gray dots/squares (west/east of 70.85°E, respectively) and pink dots are the 2008–2010 relocated seismicity and 2015 aftershocks, respectively, which are projected to profile AA' in Figure 4b. The 2009 event on the profile AA' (black star) serves as the origin point in Figure 4b. The projected events form two distinct structures dipping toward opposite directions: ~75° to the south for events west of 70.85°E (gray dots and the red dashed line), ~75° to the north for events east of 70.85°E (gray squares). The south dipping plane is subparallel to the steeper nodal plane in the focal mechanism solutions (red line in the inset).

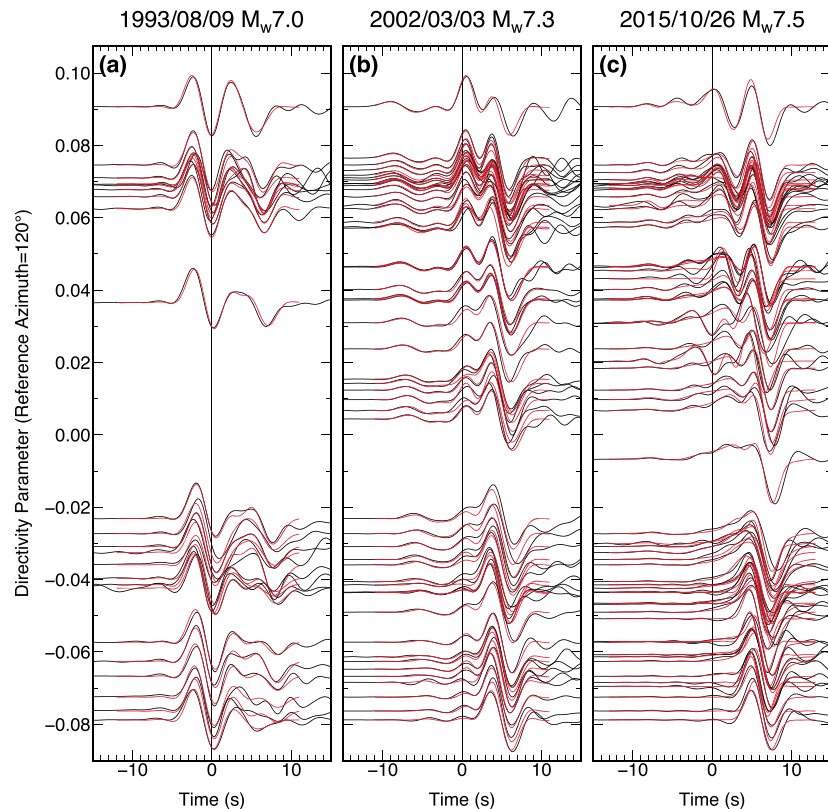


Figure 5. Waveform fits of subevent models for the (a) 1993 M_w 7.0, (b) 2002 M_w 7.3, and (c) 2015 M_w 7.5 events. The directivity parameters and alignments are the same as in Figure 3. Data and synthetics are plotted in black and red, respectively.

two smaller subevents E2 and E3 to the north. The 2002 event initiated with an $M6.6$ subevent E1, and then ruptured to the east with a bigger subevent E2, and the biggest subevent E3 ($M7.2$) near the 2009 event. E3 contributes most of the moment of the 2002 event. The 2015 event started with a $M6.4$ subevent E1 near the 2009 event, and ruptured toward $N60^\circ W$ to E2, about 30 km away. Then the rupture reversed direction and produced a $M7.3$ subevent E3. Two seconds after E3, another $M7.2$ subevent E4 occurred back near the 2009 event. A continuous rupture from E2/E3 to E4 may be unlikely considering the short time delay, so we consider E4 as a late development after E1, possibly with dynamic triggering from E2 or E3.

5. Fault Plane and Slip Rate

Despite the diverse rupture processes, the major subevent of each earthquake, 1993.E1, 2002.E3, and 2015.E4 are all located within 5 km of the 2009 event, the spatial resolution of subevent modeling. With subevents treated as point sources in our method, we cannot constrain their spatial dimensions. Therefore, to assess whether the three subevents overlap significantly, we assume a circular crack and a constant strain drop of 10^{-4} , the average value commonly suggested for earthquakes at all depths [Vallée, 2013]. We then convert the strain drop to stress drop using the shear modulus at 210 km depth in the PREM model, and estimate the rupture dimensions and average slips from the subevent moments. For the $M7.2$ subevents 2002.E3 and 2015.E4, the diameter of the fault is about 32 km and average slip is ~ 1.2 m, while for the $M6.8$ 1993.E1 the diameter is about 20 km, and average slip is ~ 0.7 m. These diameters are much larger than the offsets between the subevents. Together with the similar centroid depths and focal mechanisms estimated in section 2, we suggest that the three large subevents ruptured on the same (or closely spaced subparallel) fault patch, instead of side-by-side laterally.

The focal mechanisms estimated in section 2 suggest two possible fault planes, one dipping to the south at 70° , the other to the north at 20° . The subevent models do not provide any additional constraints on which fault plane the three large subevents recurred. In this case, we may use background seismicity and aftershocks to identify the fault plane. In Figure 4b, we project the relocated background seismicity and aftershocks of the 2015 event onto profile AA', roughly perpendicular to the fault strikes. The projected seismicity shows two clearly separated dipping structures toward the south and north, respectively, both at $\sim 75^\circ$ (Figure 4b). Note that the events east of $70.85^\circ E$ (gray squares) form the north dipping structure, while the events west of $70.85^\circ E$ (gray dots), including the 2015 aftershocks (pink dots), form the south dipping structure. Thus, we suggest that the south dipping nodal plan is the fault plane of the three large subevents.

Lister *et al.* [2008] show that deep earthquake locations and focal mechanisms in Hindu Kush support the slab-stretching model, in which earthquakes concentrate in the necking zone due to the ongoing break-off of the subducted oceanic slab. Given our new observation that $M \sim 7$ subevents may recur on the same fault plane, what would be the required slab-stretching rate? To answer this question, we calculate the cumulative slip on the fault as a function of time (Figure 6a). As discussed above, the last three $M \geq 7.0$ events likely produced average slips of 0.7 m (1993.E1) and 1.2 m (2002.E3 and 2015.E4), respectively. We further assume that the three earlier events, 1949 $M7.5$, 1965 $M7.4$, and 1983 $M7.4$, are similar to the 2002 $M7.3$ and 2015 $M7.5$ events, each contributing 1.2 m of slip on the same fault patch, and the 1974 $M7.0$ event is similar to the 1993 $M7.0$ event, contributing 0.7 m slip. Combining all these events together, we have 6.2 m cumulative slip in 66 years since the 1949 event. The best fitting average slip rate is about 9.6 cm/yr, as shown by the red line in Figure 6a. This slip rate on a 70° dipping fault translates to a vertical slab-stretching rate of 9 cm/yr, much higher than the convergence rate measured geodetically on the surface, at about 1 cm/yr [Ischuk *et al.*, 2013]. Therefore, the slab below the earthquake depth of 210 km needs to sink at 10 cm/yr to fuel the frequently recurring $M \geq 7.0$ deep earthquakes (sketched in Figure 6b). If additional aseismic deformation is involved, then the slab-sinking speed will be higher.

Slab negative buoyancy and mantle viscosity control slab-sinking speed. Seismic tomographic models show that the Hindu Kush subducted slab has not reached the high-viscosity lower mantle yet, as sketched in Figure 6b based on Figure 2 of Negredo *et al.* [2007]. If we assume that the slab necking zone is not providing significant resistance, then we can do back-of-envelope calculations about the required mantle viscosity for the slab to be sinking at 10 cm/yr. We assume the process is close to a Stokes flow, with a higher density sphere dropping through viscous fluid [Morgan, 1965]. The terminal sinking speed is given by $v = \frac{2\Delta\rho}{9\mu} gR^2$, in which $\Delta\rho$ is density contrast, μ is viscosity, g is the gravitational acceleration, and R is radius of sphere. If we take the

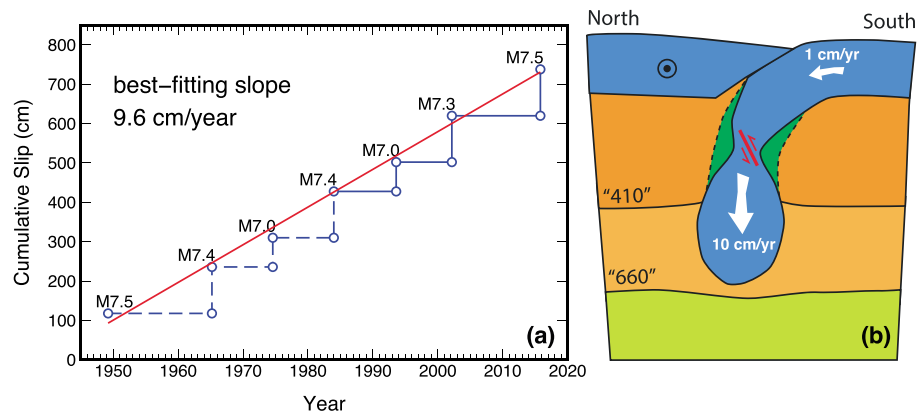


Figure 6. Slip rate and conceptual model. (a) Cumulative slip on the south dipping fault patch responsible for the main subevents of the 1993, 2002, and 2015 earthquakes. The step sizes for the three events are estimated based on subevent moments and a constant strain drop of 10^{-4} . If we assume that the earlier $M \geq 7$ events since 1949 produced similar subevents on the same fault patch, then we can extend to dashed lines. The red line shows the average slip rate of 9.6 cm/yr, much faster than the ~ 1 cm/yr convergence rate measured on the surface. (b) Conceptual model to explain the high slip rate as slab-stretching/necking effect under its negative buoyancy. The geometry of the sinking slab below the necking depth is based on the tomographic image in *Negredo et al.* [2007]. The green zone is sketched to illustrate slab geometry with no stretching, as a comparison. The slab-sinking rate needs to be 10 cm/yr to explain the average slip rate on the fault and the frequent large deep earthquakes.

average slab density anomaly to be 0.5–1%, and sphere radius to be 100 km based on tomography [*Negredo et al.*, 2007], the 10 cm/yr sinking speed requires a mantle viscosity of about 2×10^{20} Pa s. This value has the right order of magnitude for the upper mantle, especially for an active subduction zone [*Alisc et al.*, 2012], but is a few times lower than those measured from postglacial rebound in cratonic regions [*Turcotte and Schubert*, 2014]. Thus, the 10 cm/yr slab-stretching rate is physically plausible.

6. Conclusions

Out of the concentrated and anomalously frequent large deep earthquakes in Hindu Kush, we have studied the latest three $M \geq 7.0$ events in 1993, 2002, and 2015 in detail. The three events show complex and diverse rupture processes, but the main subevents/slips seem to always recur on the same fault patch, dipping 70° to the south. To explain the 10–15 year intervals between the $M \sim 7$ subevents, the average slip rate on the fault patch needs to be ~ 9.6 cm/yr, much higher than the ~ 1 cm/yr convergence rate measured on the surface. The high slip rate is likely fueled by localized slab stretching/necking [*Lister et al.*, 2008]. This requires the subducted slab below 210 km to sink at a vertical rate of 10 cm/yr, which appears to be geodynamically plausible. The inferred slab stretching may be a transient process; as the slab eventually breaks off, the seismic activity will cease and the surface will rebound [*Richards and Hager*, 1984; *Duretz et al.*, 2011].

Acknowledgments

Incorporated Research Institutions for Seismology (IRIS) provided the seismic data used in this study. We thank Thorne Lay and Lingling Ye for constructive discussions, and two anonymous reviewers for comments.

References

- Alisc, L., M. Gurnis, G. Stadler, C. Burstedde, and O. Ghattas (2012), Multi-scale dynamics and rheology of mantle flow with plates, *J. Geophys. Res.*, *117*, B10402, doi:10.1029/2012JB009234.
- Di Giacomo, D., I. Bondár, D. A. Storchak, E. R. Engdahl, P. Bormann, and J. Harris (2015), ISC-GEM: Global instrumental earthquake catalogue (1900–2009): III. Re-computed MS and mb, proxy MW, final magnitude composition and completeness assessment, *Phys. Earth Planet. Inter.*, *239*, 33–47.
- Duretz, T., T. V. Gerya, and D. A. May (2011), Numerical modelling of spontaneous slab breakoff and subsequent topographic response, *Tectonophysics*, *502*(1), 244–256.
- Gutenberg, B., and C. F. Richter (1954), *Seismicity of the Earth and Associated Phenomena*, 2nd ed., Princeton Univ. Press, N. J.
- Ischuk, A., R. Bendick, A. Rybin, P. Molnar, S. F. Khan, S. Kuzikov, S. Mohadjer, U. Saydullaev, Z. Ilyasova, and G. Schelochkov (2013), Kinematics of the Pamir and Hindu Kush regions from GPS geodesy, *J. Geophys. Res. Solid Earth*, *118*, 2408–2416, doi:10.1002/jgrb.50185.
- Lister, G., B. Kennett, S. Richards, and M. Forster (2008), Boudinage of a stretching slablet implicated in earthquakes beneath the Hindu Kush, *Nat. Geosci.*, *1*(3), 196–201.
- Morgan, W. J. (1965), Gravity anomalies and convection currents: 1. A sphere and cylinder sinking beneath the surface of a viscous fluid, *J. Geophys. Res.*, *70*(24), 6175–6187, doi:10.1029/JZ070i024p06175.
- Negredo, A. M., A. Replumaz, A. Villaseñor, and S. Guillot (2007), Modeling the evolution of continental subduction processes in the Pamir–Hindu Kush region, *Earth Planet. Sci. Lett.*, *259*(1), 212–225.

- Pavlis, G. L., and M. W. Hamburger (1991), Aftershock sequences of intermediate-depth earthquakes in the Pamir-Hindu Kush seismic zone, *J. Geophys. Res.*, *96*(B11), 18,107–18,117, doi:10.1029/91JB01510.
- Pavlis, G. L., and S. Das (2000), The Pamir-Hindu Kush seismic zone as a strain marker for flow in the upper mantle, *Tectonics*, *19*(1), 103–115, doi:10.1029/1999TC900062.
- Pegler, G., and S. Das (1998), An enhanced image of the Pamir-Hindu Kush seismic zone from relocated earthquake hypocentres, *Geophys. J. Int.*, *134*(2), 573–595.
- Poli, P., G. Prieto, E. Rivera, and S. Ruiz (2016), Earthquakes initiation and thermal shear instability in the Hindu-Kush intermediate-depth nest, *Geophys. Res. Lett.*, *43*, 1537–1542, doi:10.1002/2015GL067529.
- Prieto, G. A., G. C. Beroza, S. A. Barrett, G. A. López, and M. Florez (2012), Earthquake nests as natural laboratories for the study of intermediate-depth earthquake mechanics, *Tectonophysics*, *570*, 42–56.
- Richards, M. A., and B. H. Hager (1984), Geoid anomalies in a dynamic Earth, *J. Geophys. Res.*, *89*(B7), 5987–6002, doi:10.1029/JB089iB07p05987.
- Sippl, C., B. Schurr, X. Yuan, J. Mechie, F. Schneider, M. Gadoev, S. Orunbaev, I. Oimahmadov, C. Haberland, and U. Abdybachev (2013), Geometry of the Pamir-Hindu Kush intermediate-depth earthquake zone from local seismic data, *J. Geophys. Res. Solid Earth*, *118*, 1438–1457, doi:10.1002/jgrb.50128.
- Storchak, D. A., D. Di Giacomo, I. Bondar, E. R. Engdahl, J. Harris, W. H. K. Lee, A. Villasenor, and P. Bormann (2013), Public release of the ISC-GEM global instrumental earthquake catalogue (1900–2009), *Seismol. Res. Lett.*, *84*(5), 810–815.
- Turcotte, D. L., and G. Schubert (2014), *Geodynamics*, Cambridge Univ. Press, Cambridge, U. K.
- Vallée, M. (2013), Source time function properties indicate a strain drop independent of earthquake depth and magnitude, *Nat. Commun.*, *4*.
- Zhan, Z., D. Helmberger, M. Simons, H. Kanamori, W. Wu, N. Cubas, Z. Duputel, R. Chu, V. C. Tsai, and J.-P. Avouac (2012), Anomalously steep dips of earthquakes in the 2011 Tohoku-Oki source region and possible explanations, *Earth Planet. Sci. Lett.*, *353*, 121–133.
- Zhan, Z., H. Kanamori, V. C. Tsai, D. V. Helmberger, and S. Wei (2014), Rupture complexity of the 1994 Bolivia and 2013 Sea of Okhotsk deep earthquakes, *Earth Planet. Sci. Lett.*, *385*, 89–96.
- Zhu, L., and D. V. Helmberger (1996), Advancement in source estimation techniques using broadband regional seismograms, *Bull. Seismol. Soc. Am.*, *86*(5), 1634–1641.